Geometrically Controlled Nanoporous PdAu Bimetallic Catalysts with Tunable Pd/Au Ratio for Direct Ethanol Fuel Cells

L. Y. Chen,[†] N. Chen,[†] Y. Hou,[†] Z. C. Wang,[†] S. H. Lv,[†] T. Fujita,[†] J. H. Jiang,[‡] A. Hirata,[†] and M. W. Chen*,[†,‡,⊥]

[†]WPI-Advanced Institute for Materials Research, Tohoku University, Sendai 980-8577, Japan

[‡]State Key Laboratory of Metal Matrix Composites and School of Materials Science and Engineering, Shanghai Jiao Tong University, Shanghai 200030, China

[⊥]CREST, Japan Science and Technology Agency, Saitama 332-0012, Japan

S *Supporting Information*

ABSTRACT: We report nanoporous $Pd_{100-x}Au_x$ (x = 0, 25, 50, 75, 100; np-PdAu) bimetallic catalysts fabricated by electrochemically dealloying isomorphous $Pd_{20-y}Au_yNi_{80}$ (y = 0, 5, 15, 20) precursors. The chemical composition of the nanoporous bimetallic catalysts can be precisely controlled by predesigning Pd/Au ratios in the ternary alloys. Dealloying at an appropriate potential for each alloy can selectively leach Ni away while the Pd and Au remain intact to form a geometrically controllable nanoporous structure. The electrocatalysis of the np-PdAu shows evident dependence on the Au/Pd atomic ratio, and the $np\text{-}Pd_{75}Au_{25}$ bimetallic catalyst shows superior electrocatalytic performance toward ethanol electrooxidation in comparison with commercial Pt/C, np-Pd, and other np-PdAu alloys. Since there are no obvious geometric shape and pore size disparities among the np-PdAu samples, the dealloyed catalysts also provide an ideal system to explore the chemical origins of the excellent catalytic properties of bimetallic catalysts.

KEYWORDS: *nanoporous alloy, dealloying, bimetallic catalysis, direct ethanol fuel cell, surface electronic structure, Pd–Au catalyst*
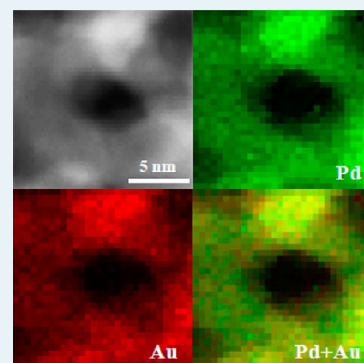
1. INTRODUCTION

Electrocatalytic energy conversion plays a vital role in the development of sustainable technologies for decreasing consumption of fossil fuels and mitigating climate warming.[1−5] Fuel cells can convert the chemical energy of small molecule fuels into electricity through chemical reactions with oxygen.[6,7] The energy efficiency of fuel cells can yield up to 85%, which is much higher than conventional internal combustion engines due to Carnot cycle limitation (<35%).[8−10] Among main fuel molecules, ethanol has many advantages in comparison with hydrogen, methanol, and formic acid because it has less toxicity, more production, and a higher energy density.[11−19] In contrast with methanol and hydrogen, which can produce only six and two electron transfers during the oxidation, the complete electrocatalytic oxidation of ethanol can generate twelve electron transfers, which results in an exceptionally high energy density of ~29.7 MJ/kg.[20] Thus, direct ethanol fuel cells (DEFCs) have recently attracted considerable attention for applications in mobile devices and vehicles for which a large specific energy is required.[20−29] It has been found that reaction media strongly influence the electrocatalytic oxidation of ethanol. The oxidation of ethanol in acidic media shows slow kinetics due to catalyst poisoning by reaction intermediates. Acetaldehyde, acetic acid, and carbon monoxide, detected by in situ oxidation experiments, are readily adsorbed on the active sites of catalysts and reduce the reaction efficiency and selectivity.[30−32] Recently, it was found that an alkaline medium

is advantageous to enhance the kinetics of ethanol oxidation reactions, and sufficient hydroxyl groups can weaken the adsorption of carbonyl species at the interface for the relief of catalyst poisoning.[8,33]

The catalyst is vital to the small-molecule oxidation at the anode. The platinum-based alloys are widely used as catalysts in fuel cells because of their high catalytic performance;[11,30,34−45] however, the high cost of platinum is one of the major reasons that restrict the wide-range applications of fuel cell technology. Developing platinum-free fuel cells has been the current topic of intense investigations.[46−58] An additional advantage of the alkaline media for electrocatalytic oxidation reaction of ethanol is that naturally abundant palladium possesses a higher catalytic activity for ethanol electrooxidation in an alkaline electrolyte than platinum.[11,23,59,60] The catalytic activity and stability of Pd catalysts can be further enhanced by forming bimetallic Pd-based catalysts. It has been reported that PdNi, PdFe, and PdCu alloys possess improved catalytic performance in the oxygen reduction reaction (ORR).[61−63] PdSn bimetallic catalysts exhibit a better activity toward ethanol oxidation.[8] Recently, nanoparticulate PdAu catalysts have been verified to possess highly enhanced catalytic activity toward ethanol oxidation in alkaline electrolytes,[64−70] and addition of Au is
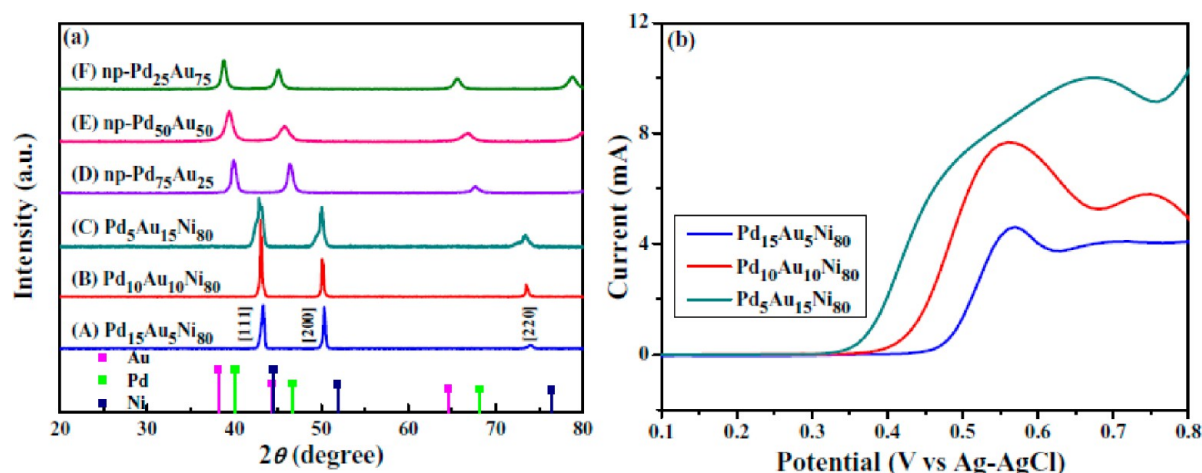
Figure 1. (a) XRD patterns of PdAuNi precursors (A) $Pd_{15}Au_5Ni_{80}$, (B) $Pd_{10}Au_{10}Ni_{80}$, (C) $Pd_5Au_{15}Ni_{80}$ and corresponding as-dealloyed nanoporous PdAu bimetallic alloys (D) np-$Pd_{75}Au_{25}$, (E) np-$Pd_{50}Au_{50}$, and (F) np-$Pd_{25}Au_{75}$. (b) Anodic polarization curves of three PdAuNi precursors in 0.5 M H_2SO_4. The polarization scan rate is 5 mV/s.

expected to improve the selectivity and stability of Pd catalysts in alkaline media.

The enhanced catalysis of bimetallic catalysts arises mainly from two interface effects: ligand and ensemble effects.[71,72] The ligand effect refers to the change of catalytic properties due to electronic interactions between two metallic elements,[73−76] whereas the ensemble effect results from surface atomic arrangements and surface strains.[71,77,78] Fundamentally, both effects are associated with the chemical composition and geometric shape of catalysts. However, it is difficult to simultaneously control both composition and geometry of nanoparticulate catalysts to achieve optimal catalytic performance. In this study, we develop nanoporous PdAu (np-$Pd_{100−x}Au_x$, x = 0, 25, 50, 75, 100) catalysts with well-controlled chemical composition and nanopore size by electrochemically dealloying $Pd_{20−y}Au_yNi_{80}$ (y = 0, 5, 10, 15, 20) precursors. The catalytic activities of np-PdAu show strong dependence on the atomic ratio of Pd and Au, indicating that the strong interface effect evidently influences the catalytic activity of np-PdAu catalysts. Moreover, the np-PdAu catalyst with an optimal composition of $Pd_{75}Au_{25}$ possesses superior catalytic activity toward ethanol oxidation.

2. RESULTS AND DISCUSSION

2.1. Precursors for Dealloying. To obtain a uniform nanoporous structure of np-PdAu by dealloying, it is essential to choose suitable precursors that must satisfy two basic requirements: a homogeneous single phase and large potential difference[79−81] between the reserved Pd (Au) and the leached element. In this study, we select $Pd_{20−y}Au_yNi_{80}$ ternary alloys as the precursors. The standard electrode potentials of Pd, Au, and Ni are 0.915, 1.498, and −0.257 V, respectively. The large potential difference between Pd and Ni (1.172 V) as well as Au and Ni (1.755 V) offers a wide potential range for selectively etching Ni from the ternary precursors. The residual composition of Pd and Au in np-PdAu catalysts can be predetermined when preparing precursor alloys, which is favorable to the development of bimetallic catalysts with designated compositions. The X-ray diffraction (XRD) patterns shown in Figure 1a verify that three $Pd_{20−y}Au_yNi_{80}$ ribbons for dealloying precursors are a uniform single-phase solid solution. All the diffraction peaks can be indexed as a face-centered cubic

(fcc) phase with crystal planes of (111), (200), (220). In comparison with pure Ni, the diffraction peaks of the $Pd_{20−y}Au_yNi_{80}$ precursors obviously move to the smaller diffraction angles. The more Au content the $Pd_{20−y}Au_yNi_{80}$ precursor contains, the lower the angles that the diffraction peaks shift to, which reveals that the lattice constants of the $Pd_{20−y}Au_yNi_{80}$ alloys are larger than that of pure Ni as a result of the substitution of Au and Pd with larger atomic radii. The Pd−Au−Ni ternary phase diagram shown in Supporting Information Figure S1a indicates that Pd, Au, and Ni can form an isomorphous alloy with a simple face-centered cubic structure in the entire composition range when cooling from a liquid state at high temperatures to a solid state at room temperature. The phase diagram of the Pd−Au binary system shown in Supporting Information Figure S1b further reveals that Pd and Au can constitute PdAu single-phase alloys regardless of the gold content, which provides a theoretical basis for fabrication of uniform nanoporous bimetallic PdAu with tunable compositions.

2.2. Critical Potential for Electrochemical Dealloying. To obtain np-PdAu by electrochemical dealloying, the critical potential is a key parameter for different precursor alloys. When the applied potential is sufficiently higher than the dissolution overpotential of a less noble component but lower than the dissolution overpotentials of the noble components, the less noble metal can quickly dissolve, and the noble component forms a nanoporous structure. If the applied potential is too low, even if higher than the dissolution overpotential of less noble components, the noble component may enrich on the surface to form a passivation layer, leading to the rapid decay of the etching current.[82−84] The potential between passivation and selective dissolution is called the critical potential. The generalized polarization curves of the $Pd_{20−y}Au_yNi_{80}$ alloys are illustrated in Figure 1b. At a low potential, the dissolution current is small but constant. Close to the critical potential, the dissolution current rises exponentially. Since the critical potential is sensitive to the sweep rates and compositions of the precursor alloys and electrolytes, it usually falls into a narrow range, rather than a well-defined value. In this study, the critical potentials of $Pd_{15}Au_5Ni_{80}$, $Pd_{10}Au_{10}Ni_{80}$, and $Pd_5Au_{15}Ni_{80}$ for dealloying in 0.5 M H_2SO_4 are 0.47, 0.42, and 0.36 V, respectively. With the increase in the Au contents
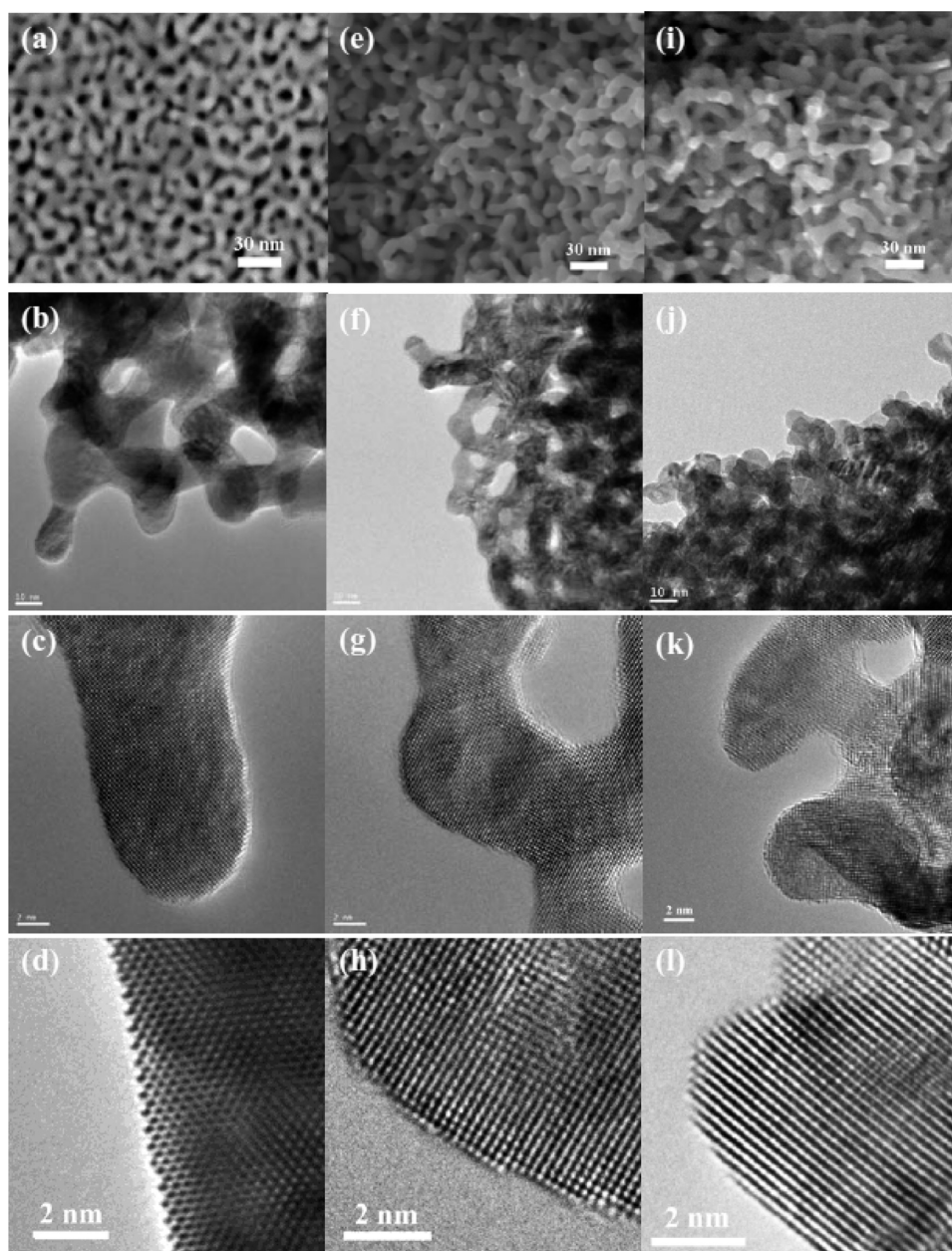
Figure 2. SEM, TEM, and HRTEM images of (a−d) np-Pd$_{75}$Au$_{25}$, (e−h) np-Pd$_{50}$Au$_{50}$, and (i−l) np-Pd$_{25}$Au$_{75}$.

in the ternary alloys, the critical potential gradually decreases, although the standard electrode potential of Au is higher than that of Pd and Ni.

2.3. Microstructure of np-PdAu. Figure 1a also exhibits the XRD diffraction spectra of the np-PdAu samples with different composition fabricated by dealloying Pd$_{20-y}$Au$_y$Ni$_{80}$ in a H$_2$SO$_4$ solution at the corresponding critical potentials. The leaching of Ni results in the downshift of the np-PdAu diffraction, and all the diffraction peaks of the dealloyed np-PdAu can be indexed by the fcc structure. The positions of the diffraction peaks of np-PdAu are at intermediate values between pure Pd and Au, indicating the formation of Pd and Au solid solutions. On the basis of the XRD patterns, the lattice constants of np-Pd$_{75}$Au$_{25}$, np-Pd$_{50}$Au$_{50}$, and np-Pd$_{25}$Au$_{75}$ are measured to increase gradually from 3.880 to 4.030 Å. The linear relationship between the lattice constants and the Au mole fraction is consistent with the predetermined component

in the precursors. The complete disappearance of all the peaks of the precursors suggests that the initial Pd$_{20-y}$Au$_y$Ni$_{80}$ phases have changed to be uniform np-PdAu alloys with designated Au concentrations.

The microstructures of as-dealloyed np-PdAu alloys are shown in Figure 2. The metallic ligaments and nanoporous channels are bicontinuously distributed across the entire samples, as exhibited by the scanning electron microscopy (SEM) images (Figure 2a, e and i). The pore sizes of the dealloyed np-Pd$_{100-x}$Au$_x$ (x = 25, 50, 75) are all approximately ~10 nm, verified by rotational fast Fourier transform. The similar porosity results probably because the formation of nanoporosity of the bimetallic catalysts is mainly controlled by the interface diffusion of Pd, which is much slower than that of Au.[85] Transmission electron microscope (TEM) images (Figure 2b, f and j) further reveal the nanoporosity of the binary np-Pd$_{100-x}$Au$_x$ sample, which can be identified by the
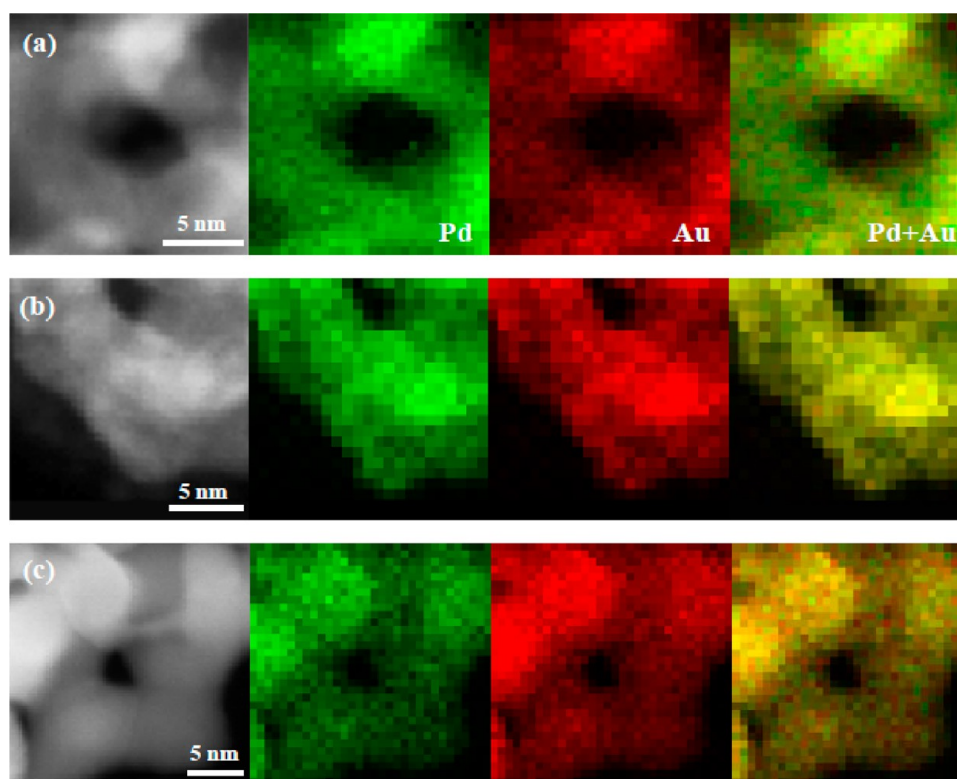
Figure 3. STEM-EDS mapping of as-prepared (a) np-Pd$_{75}$Au$_{25}$, (b) np-Pd$_{50}$Au$_{50}$, (c) np-Pd$_{25}$Au$_{75}$. (Left to right: dark field image, Pd mapping, Au mapping, Pd−Au overlay mapping.)
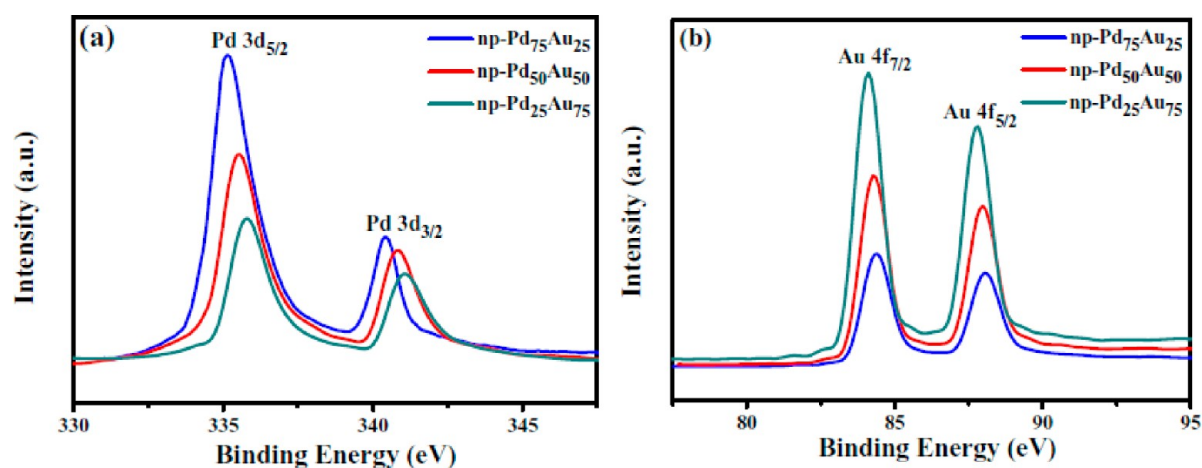

Figure 4. XPS characterization of as-prepared np-PdAu. XPS spectrum of (a) Pd 3d and (b) Au 4f.

contrast difference between dark metal skeletons and bright pore channels. The atomic structure of np-PdAu is investigated by using high resolution TEM (HRTEM). Figure 2c, g and k are the representative HRTEM images of the bimetallic ligaments, which illustrate that the specimens have a good crystalline structure with well-defined lattice fringes. Most of the exposed facets of the ligaments are (111) and (100) planes with a high density of atomic steps (Figure 2d, h and l), regardless of compositions, which is similar to that of dealloyed nanoporous gold.[86] Consequently, all Pd$_{20-y}$Au$_y$Ni$_{80}$ precursors can be successfully dealloyed for the formation of a uniform nanoporous structure with tunable compositions but similar porous geometries and nanopore sizes.

From the STEM-energy dispersive X-ray spectroscopy (EDS) mapping indicated in Figure 3a−c, we can observe that Pd and Au atoms are uniformly distributed in the ligaments, regardless of np-Pd$_{75}$Au$_{25}$, np-Pd$_{50}$Au$_{50}$, and np-Pd$_{25}$Au$_{75}$. To illustrate possible surface segregation of one constituent component, we constructed the overlap chemical mappings of Pd and Au for each bimetallic alloy. Although the mixing color is dependent on the ratio of Pd and Au and corresponds to the Pd-rich or Au-rich samples, one cannot find detectable surface segregation of either Au or Pd, suggesting uniformly mixed Au and Pd surfaces of the bimetallic nanoporous alloys. Moreover, quantitative EDS analyses show that the average atomic ratios of Pd and Au of the dealloyed
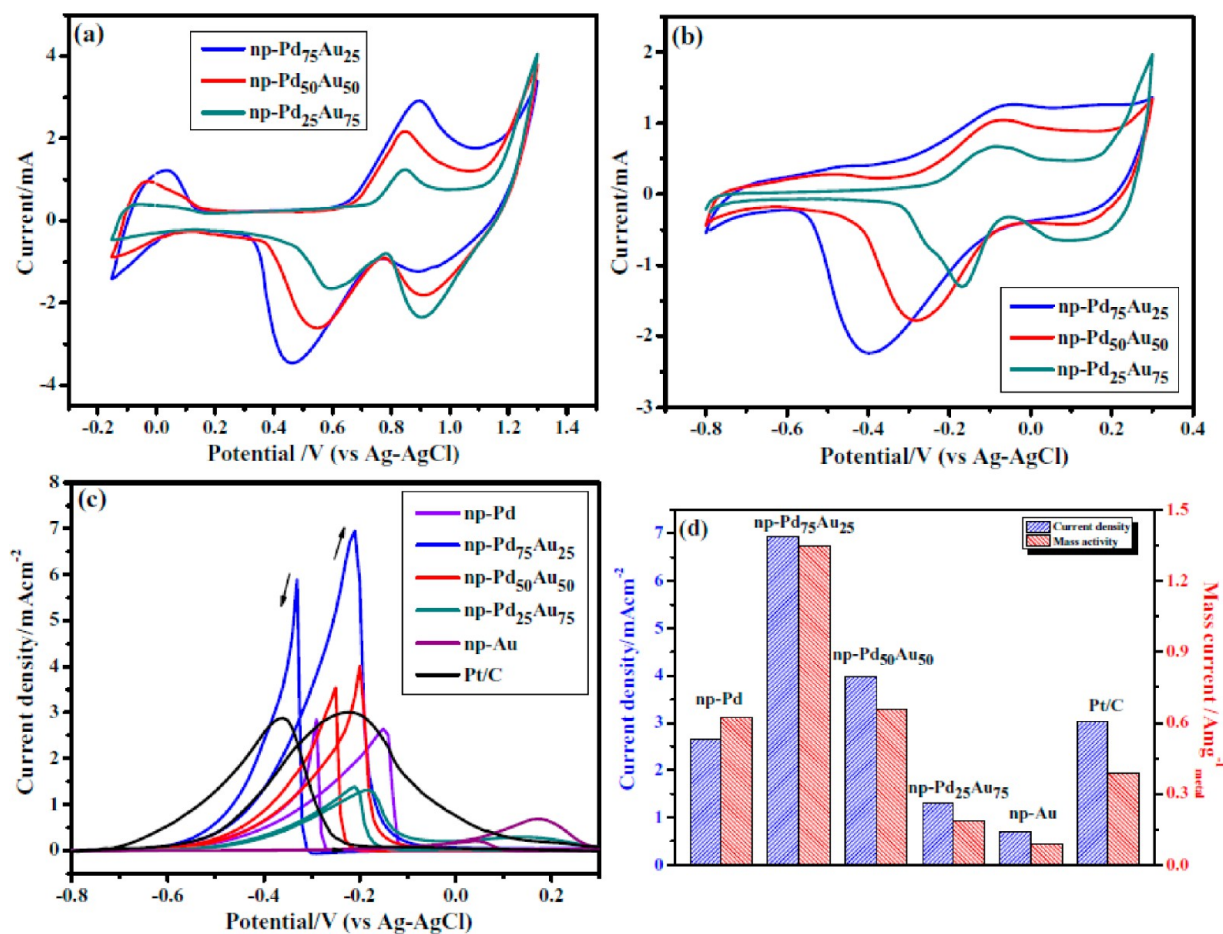
Figure 5. Electrochemical characterization of dealloyed np-PdAu. (a) CV curves of np-PdAu catalysts in 0.5 M H_2SO_4. (b) CV curves of np-PdAu catalysts in 1.0 M KOH. (c) Normalized CV curves of 0.5 M ethanol in 1.0 M KOH solution on np-PdAu and np-Pd catalysts, respectively. (d) Current densities and mass activities for ethanol oxidation in 1.0 M KOH solution on np-PdAu, np-Pd, and Pt/C. Scan rate: 50 mV/s.

samples are very close to their nominal compositions predetermined in the precursor alloys.

We also measured the surface chemistry of as-dealloyed bimetallic nanoporous PdAu alloys using X-ray photoelectron spectroscopy (XPS). Figure 4 exhibits the Pd 3d and Au 4f core level spectra of the np-PdAu alloys. The two peaks shown in Figure 4a can be assigned to the Pd $3d_{3/2}$ (high-energy band) and $3d_{5/2}$ (low-energy band) spin−orbit states of zero-valent Pd. The binding energies of Pd $3d_{5/2}$ for np-$Pd_{75}Au_{25}$, np-$Pd_{50}Au_{50}$, and np-$Pd_{25}Au_{75}$ are 335.1, 335.5, and 335.7 eV, respectively, which are visibly higher than that of pure Pd (335.0 eV) and shift to large values with the decrease in the Pd/Au ratios. This is consistent with previous observations.[87,88] Meanwhile, the binding energies of Au $4f_{7/2}$ for np-$Pd_{75}Au_{25}$, np-$Pd_{50}Au_{50}$, and np-$Pd_{25}Au_{75}$ shown in Figure 4b are at 84.4, 84.3, and 84.1 eV, which are much higher than that of pure Au (83.8 eV) but increase with the Au/Pd ratios. The shift of the binding energies of Pd and Au in np-PdAu from pure elements indicates the evident change in the electronic structure, particularly the d band modification of Pd, due to intra-atomic charge transfer or interatomic charge transfer between Au and Pd when they are alloyed together in the nanoporous structure. The surface compositions of np-$Pd_{75}Au_{25}$, np-$Pd_{50}Au_{50}$, and np-$Pd_{25}Au_{75}$ determined by XPS analysis are $Pd_{79}Au_{21}$, $Pd_{56}Au_{44}$, and $Pd_{23}Au_{77}$, respectively. The very small deviation between the surface compositions, determined by XPS, and the nominal

bulk ones further suggests the inconsequential surface segregations in the bimetallic PdAu catalysts.
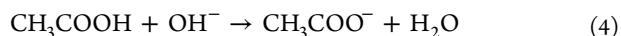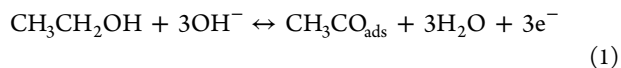
2.4. Voltammetric Characterization of np-PdAu. The electrochemical properties of the np-PdAu were characterized in both acid and alkaline solutions by means of cyclic voltammetry (CV). Figure 5a shows the normalized CV curves of the np-PdAu catalysts in a 0.5 M H_2SO_4 solution at a scan rate of 50 mV·s^{-1}. The invariability of voltammetry during several cycles suggests that the surface layers of the dealloyed samples have already been stabilized during leaching of nickel atoms from the precursor alloys. The peaks in the region between −0.15 and 0.05 V can be attributed to the adsorption and desorption of hydrogen by Pd. The characteristic hydrogen adsorption/desorption peaks gradually decrease in intensity with the decrease in the Pd/Au ratios. With the scans moving to the high potential region, the broad oxidation peaks appear from the potential of 0.65 V as a result of the formation of Pd and Au surface oxides. Subsequently, the two reduction peaks appear during the negative scans. The corresponding peaks at 0.5 and 0.9 V are ascribed to the reduction of the Pd oxide and Au oxide, respectively. The detectable negative shift of the palladium oxide reduction peak takes place with the decrease in the gold contents, demonstrating the catalytic activity of Pd is significantly modified by Au. Moreover, the intensities of the formation and reduction peaks of gold surface oxide evidently increase with the Au contents in the alloys while palladium signals decrease, indicating the fractions of surface oxides are

consistent with their bulk concentrations and, again, surface segregation can be ignored in the nanoporous bimetallic catalysts.

The CV properties of np-PdAu were also investigated in 1.0 M KOH solution (Figure 5b). Typical redox peaks associated with the oxidation/reduction of Au−Pd alloys can be observed. The formation of Pd and Au surface oxides starts from −0.2 V, −0.15 V, and −0.05 V for np-$Pd_{75}Au_{25}$, np-$Pd_{50}Au_{50}$ and np-$Pd_{25}Au_{75}$, respectively, which take place at more negative potentials than that in acidic media. Subsequently, the corresponding single oxygen desorption of Pd and Au surface oxides occurs at −0.4 V, −0.28 V, and −0.15 V, further demonstrating the relatively homogeneous distribution of Au and Pd atoms on the surfaces of bimetallic catalysts. The oxygen desorption peaks can be observed to gradually shift to higher potentials as the Au content increases, suggesting that the bulk compositions of the bimetallic catalysts strongly influence the surface activity. The electrochemically active surface areas (ECAS) can be calculated by measuring the Coulombic charges for oxygen desorption on Pd−Au surface using corresponding conversion values.[65]

2.5. Ethanol Electro-Oxidation on np-PdAu Catalysts. Free-standing nanoporous alloys are advantageous for free transport of medium molecules and electrons because of their large surface areas, bicontinuous nanoporosity, and excellent conductivity, which are particularly appropriate for electrocatalysis.[89] The interface effects on electrocatalysis can be determined by investigating the catalytic activity for ethanol oxidation in an alkaline electrolyte, which is helpful to clarify the synergistic effect between metal components as the composition changes. The complete ethanol oxidation can transfer 12 electrons during the reaction. The in situ FTIR observation shows that the selectivity from ethanol to CO_2 is relatively low. The ethanol oxidation in alkaline media mainly corresponds to the following mechanisms:

$$CH_3CH_2OH + 3OH^- \leftrightarrow CH_3CO_{ads} + 3H_2O + 3e^- \tag{1}$$

$$OH^- \leftrightarrow OH_{ads} + e^- \tag{2}$$

$$CH_3CO_{ads} + OH_{ads} \rightarrow CH_3COOH \tag{3}$$

$$CH_3COOH + OH^- \rightarrow CH_3COO^- + H_2O \tag{4}$$

It has been suggested that the rate-determining step in the ethanol oxidation reaction is eq 3. The catalytic activity of Pd-based catalysts strongly depends on the pH value of electrolytes. The oxidation reaction is much faster in alkaline media than in acidic ones because continued dehydrogenation of ethanol cannot readily proceed in acidic media due to the lack of OH species that can instantly remove hydrogen.[21,22]

Figure 5c displays the catalytic performance of the as-dealloyed np-PdAu catalysts toward ethanol electrooxidation. For comparison, the monometallic np-Pd and np-Au are fabricated by etching the $Pd_{20}Ni_{80}$ alloy and $Au_{20}Ni_{80}$ in 0.5 M H_2SO_4 electrolyte at a potential of 0.5 and 0.35 V, respectively. The morphology and pore size of np-Pd are similar to np-$Pd_{75}Au_{25}$. All the current densities are normalized by ECAS. Each CV curve has two well-defined current peaks during the forward and negative scans. The oxidation peak in forward scan can be attributed to the oxidation of freshly chemisorbed species from ethanol adsorption, and the oxidation peak in negative scan means the removal of carbonaceous species incompletely oxidized in the forward scan. As a result, the ratio

of the forward current density peak (I_f) to the backward current density peak (I_b) reflects the tolerance ability to carbonaceous species accumulation. A high ratio I_f/I_b indicates efficient oxidation of ethanol during the forward scan and little accumulation of carbonaceous residues. As shown in Table 1, the np-$Pd_{75}Au_{25}$ and np-$Pd_{50}Au_{50}$ have higher I_f/I_b values than others, which reveals the higher catalytic efficiency for direct oxidation during the forward scan.

**Table 1. The E_f, E_{onset}, I_f, and I_s of Ethanol Electrooxidation on the Different Catalysts**

catalyst	E_{onset}, V vs Ag−AgCl	E_f, V vs Ag−AgCl	I_f, mA cm^{-2}	I_f/I_b
np-Pd	−0.52	−0.15	2.65	0.96
np-$Pd_{75}Au_{25}$	−0.58	−0.21	6.95	1.18
np-$Pd_{50}Au_{50}$	−0.55	−0.20	4.0	1.13
np-$Pd_{25}Au_{75}$	−0.50	−0.18	1.31	0.94
np-Au	−0.1	0.17	0.69	
Pt/C	−0.58	−0.22	3.02	1.04

In addition, different from others, the CV curve on np-$Pd_{25}Au_{75}$ exhibited the broad peak between 0.1 and 0.3 V, which can be attributed to the rich Au atoms on the surface of the np-$Pd_{25}Au_{75}$ catalyst for direct ethanol oxidation. The catalytic activity of Au is obvious far lower than that of Pd. Without Pd, the ethanol oxidation reaction on np-Au only occurs between 0.1 and 0.3 V. From Figure 5c and Table 1, one can see the onset potential (E_{onset}) of np-$Pd_{75}Au_{25}$ (−0.58 V) slightly downshifts compared with that of np-Pd (−0.52 V). The shift of E_{onset} to a more negative value indicates that np-$Pd_{75}Au_{25}$ can enhance the electrooxidation kinetics of ethanol, which is important for fuel cell applications. It can also be observed that the forward peak potentials (E_f) of ethanol oxidation on np-$Pd_{75}Au_{25}$ and np-$Pd_{50}Au_{50}$ are more negative than that of np-Pd. The negative shift of E_f can be attributed to the modification of the Pd d band electronic structure by Au alloying. The lower peak potential gives rise to a lower activation barrier toward ethanol oxidation. The E_f gradually increases with the Au content during the forward scan. The magnitude of the anodic peak current in the forward scan is proportional to the amount of ethanol oxidized on catalysts. As shown in Figure 5d, the ECSA-normalized current density of np-$Pd_{75}Au_{25}$ exhibits a higher value than commercial Pt/C, np-$Pd_{50}Au_{50}$, pure np-Pd, np-$Pd_{25}Au_{75}$, and np-Au. In comparison with other reported Pd-based catalysts, such as Pd nanoparticles,[90] PdAu nanodendrites,[91] and PdAu core−shell compsites,[92] the np-$Pd_{75}Au_{25}$ also shows a higher current density, demonstrating the superior electrocatalytic activity of np-$Pd_{75}Au_{25}$ toward the electrooxidation of ethanol. The high electrocatalytic activity of np-$Pd_{75}Au_{25}$ can also be confirmed by the metal mass normalized-current densities (Figure 5d).

It has been known that the addition of Au into Pd catalysts can enhance catalytic activity and selectivity as well as the resistance to poisoning.[65,67,93] During the electrocatalytic ethanol oxidation in alkaline media, CO_{ads} can be produced by carbon−carbon bond breaking. The intermediate species strongly adsorb on the active sites of catalysts and hinder the reaction.[94] The previous study shows that Au enhances the activity and poisoning tolerance of Pd for alcohol oxidation as a result of an ensemble effect. Au is a good catalyst for CO

oxidation. The CO_{ads} can be oxidized by the following reactions in alkaline medium.[95]

$$CO_{ads} + Au-OH_{ads} \rightarrow Au-CO-OH \rightarrow Au-COOH$$
$$\rightarrow Au + CO_2 + H_2O \quad (5)$$
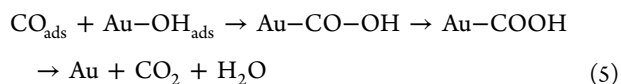
One hypothesis is that Pd acts as primary active sites for the degradation and dehydrogenation of alcohol and the Au surface can oxidize CO-like intermediate species to produce CO_2, releasing the active sites. For the nanoporous Pd–Au catalysts, the surface Au atoms have strong interaction with the Pd atoms and result in the ligand effect of Pd and Au. The synergistic effect between Pd and Au can modify the electronic property of Pd surface layer to form different circumstances for electro-catalytic reactions. The very similar porous geometry among the bimetallic catalysts also suggests that the enhanced catalysis arises mainly from the chemical composition difference, which provides experimental benchmarks for theoretically under-standing the bimetallic effect.

To evaluate the electrocatalytic endurance, the chronoam-perograms of the np-PdAu alloys, pure np-Pd, and commercial Pd/C toward ethanol electrooxidation were investigated at −0.2 V at room temperature. As shown in Figure 6, the Au
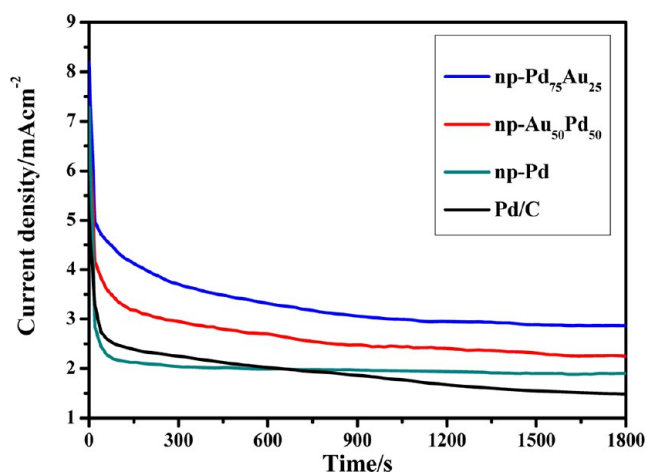

Figure 6. Chronoamperograms of the np-PdAu alloys and pure np-Pd toward ethanol electrooxidation at a potential of −0.2 V.

addition can dramatically reduce the current decay rate and keep the high electrocatalytic activities of np-$Pd_{75}Au_{25}$ and np-$Pd_{50}Au_{50}$ for much longer times than np-Pd and commercial Pd/C. This is probably because the gold component can effectively prevent the poisoning of the intermediate species. Therefore, the incorporation of Au into Pd catalysts can enhance not only the electrocatalytic activity but also the electrocatalytic stability toward ethanol oxidation.

2.6. Surface Atomic Structure and Electronic Proper-ties. To gain more insights into the physical mechanism underlying the different catalytic properties and the electronic nature of the Pd–Au systems, we further conducted a comprehensive density functional theory (DFT) calculations by taking into account the Au concentrations, the optimum absorption location, and structural relaxation.

In this work, a series of substitution concentrations of Au for Pd are considered, together with all possible substitution sites. The calculation results indicate that the Pd–O connection configuration is always energetically more stable than the Au–O, independent of the substitution concentration of Au, which

demonstrates that the ethanol is prone to be decomposed on top of the Pd atoms on the bimetallic surfaces. Figures 7a–e
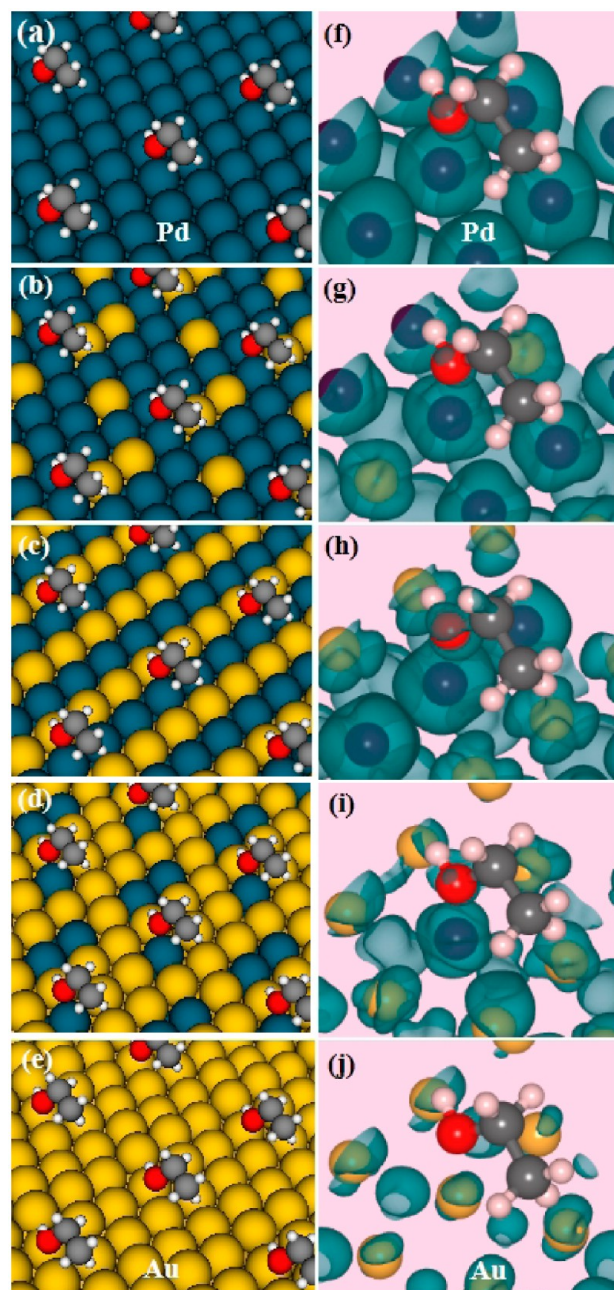

Figure 7. (a–e) Surface models with different atomic ratios of Pd/Au used for modeling ethanol catalysis. (f–j) Corresponding isosurface plots in the energy window (E_F −0.01 eV, E_F +0.01 eV). The atomic ratio of (a, f) Pd; (b, g) Pd/Au = 3: 1; (c, h) Pd/Au = 1: 1; (d, i) Pd/Au = 1: 3; (e, j) Au. The blue and yellow balls represent Pd and Au atoms; the gray, red, and white balls represent the C, O, and H atoms in the ethanol molecule, respectively.

show the five optimized models for the ethanol catalysis systems, in which the Au concentration varies from 0 to 1.0 by an interval of 0.25. The relaxed bond length between Pd (Au in pure Au surface) and O is 2.482, 2.434, 2.516, 2.641, and 3.097 Å when the Au concentration is 0, 0.25, 0.5, 0.75, and 1.0, respectively. The shortest length of Pd–O bond is observed from the catalyst with 0.25 Au, indicating that the Pd–O is the strongest bond in this case. This also suggests that the largest
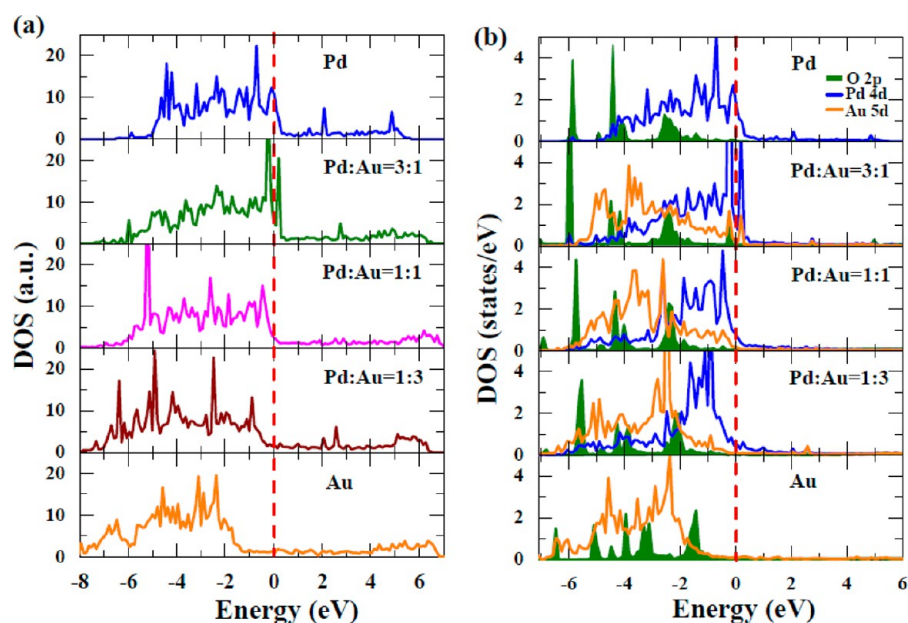
Figure 8. (a) Total densities of states (DOS) of the surface catalysis models for different concentrations of Au. (b) Projected densities of states (DOS) plots of the O in the ethanol, the Pd directly contacting the O (Au in pure Au surface), and the Au nearest to the Pd for the surface catalysis models with different concentrations of Au. The vertical lines indicate the Fermi level.

level of hybridization occurs between the Pd and O when the Au fraction is 0.25, which can well explain the optimum catalysis efficiency of $Pd_{75}Au_{25}$ observed from the experiments. Such a difference in local atomic bonding structure raises an appealing possibility that different electronic properties can be controlled by manipulating the Au concentration.

Figure 8a shows total density of states (DOS) of the PdAu catalysts with different concentrations of Au. The electronic states obviously change with the Au concentrations, indicating a strong effect of Au on the catalysis of the PdAu catalysts. As the Au concentration increases, the electronic states below the Fermi level (E_F) are shifted to a lower energy region, which can be attributed to the higher Fermi level of metallic Au, as compared with that of Pd. Detailed projected DOS (PDOS) analyses of the O, Pd, and Au atoms in each case reveal that the electron states at E_F originate mainly from the d orbitals of Pd (Figure 8b). Evidently, the d states of Pd at E_F decrease largely with the increase in the Au concentration. Moreover, the electron states of O 2p are located below E_F, which is hybridized with the d orbitals of Pd (Au). However, the highest degree of orbital hybridization rests with the system with a ratio of Pd to Au of 0.25, in agreement with the above bond-length analysis.

To investigate how the electrons distribute around E_F, the electron-density isosurfaces near E_F for the models with different Pd/Au ratios are shown in Figure 7f–j. One can see that the charges surrounding Pd and Au are connected in each case and broadly distributed in the whole surface. Another feature is that once the Au is introduced, different numbers of accumulated electrons appear around the Pd and Au atoms: the charges on the Pd atoms are heavier than those on the Au atoms (Figure 7g–i), which is consistent with the total DOS analyses.

In summary, the atomic structures and electronic properties of the ethanol catalytic systems exhibit strong dependence on the atomic ratios of Pd to Au. The preferred sites for ethanol lying above the Pd (111) surface are determined, and the most stable structure is obtained by taking into account the structural relaxation. The electronic structures of the pure Pd (111) surface differ largely from those of Au-substituted systems, which is expected to trigger different catalytic efficiencies and be responsible for the Pd/Au ratio dependence of the catalytic performances.

3. CONCLUSIONS

We have developed nanoporous PdAu bimetallic catalysts with tunable Pd/Au ratios by electrochemically dealloying $Pd_{20-y}Au_yNi_{80}$ (y = 0, 5, 10, 15, 20) isomorphous alloys. The catalytic activities of np-PdAu with uniform chemical distribution are strongly dependent on the atomic ratio of Pd and Au, whereas the geometric shape and size of the nanoporous alloys remain nearly constant, which provides a model system for exploring bimetallic effects on catalysis. In the nanoporous Pd–Au system, the np-$Pd_{75}Au_{25}$ is found to possess superior catalytic properties toward ethanol electro-oxidation in comparison with np-Pd, commercial Pt/C catalysts, and other np-PdAu alloys. The excellent electro-catalytic activities achieved from the optimal Pd/Au ratio arise mainly from the modified electron structure of Pd by Au alloying and the ensemble effect of the dilution of surface Pd by Au. In addition, Au plays a key role in the electrocatalytic stability of the dealloyed np-PdAu bimetallic catalysts toward ethanol electrooxidation.

4. EXPERIMENTAL SECTION

4.1. Fabrication of np-PdAu Alloys. All chemicals were used as received without any further purification. Single-phase $Pd_{20-y}Au_yNi_{80}$ (y = 0, 5, 10, 15, 20) precursors in the form of ~10 μm thick ribbons were prepared by a melt spinning method under a high-purity argon atmosphere. Np–$Pd_{100-x}Au_x$ (x = 0, 25, 50, 75, 100) catalysts were fabricated by electrochemically etching the single-phase $Pd_{20-y}Au_yNi_{80}$ (y = 0, 5, 10, 15, 20) precursors in a 0.5 M H_2SO_4 solution using an electrochemical workstation (Ivium Technology) in a standard

three-electrode cell with a Ag-AgCl electrode as the reference electrode and a Pt foil as the counter electrode. The dealloying process is controlled by a single-parameter, that is, the applied potentials. The dealloying current gradually decreases with the dealloying time at a designed potential. We set up a current threshold of 0.1 μA cm^{-2} to terminate the dealloying instead of time and etching depth. At this threshold current, the dealloying has been nearly completed, and uniform nanoporosity through entire samples can be observed by cross-sectional SEM. The dealloyed samples were rinsed by deionized water (18.2 MΩ·cm) more than three times to remove the residual chemical substances within the nanopore channels.

4.2. Microstructure Characterization. XRD patterns of dealloyed np-Pd$_{100-x}$Au$_x$ samples and Pd$_{20-y}$Au$_y$Ni$_{80}$ precursors were recorded using a Rigaku X-ray diffractometer with Cu Kα radiation (λ = 0.154 05 nm). The microstructure and chemical compositions of the as-synthesized np-Pd$_{100-x}$Au$_x$ were characterized by a JEOL JIB-4600F SEM equipped with an Oxford energy dispersive X-ray spectroscopy (EDS). A JEOL JEM-2100F TEM with an acceleration voltage of 200 kV was employed to characterize the nanoporosity and crystal structure of dealloyed samples. XPS (AxIS-ULTRA-DLD) with an Al Kα (mono) anode was utilized at an energy of 150 W in a vacuum of 10^{-7} Pa.

4.3. Evaluation of Electrooxidation Activities of np-PdAu Catalysts. All electrochemical experiments were carried out at room temperature. The solutions were purged with high-purity nitrogen (99.999%) for 20 min prior to the tests. Cyclic voltammograms of electrooxidation on np-Pd$_{100-x}$Au$_x$ catalysts were recorded by using a 1.0 M KOH solution with 1.0 M ethanol. For comparison, the commercial Pt/C (20 wt %, Johnson Matthey) catalyst was also used as a reference for the electrooxidation measurements.

4.4. DFT Calculation of Surface Atomic Structure and Electronic Property. Atomic structure and electronic property of the bimetallic PdAu catalysts were simulated using the Vienna ab initio simulation package (VASP) within the framework of density functional theory.[96] The projector-augmented wave (PAW) method[97] was used for the electron–ion interactions, and the generalized gradient approximation (GGA) by Perdew, Burke, and Ernzerhof (GGA-PBE)[98] was used to describe the exchange-correlation functional. The single particle Kohn–Sham wave function was expanded using plane wave with a cutoff energy of 400 eV, and the irreducible Brillouin zone was sampled with a regular 6 × 6 × 1 Monkhorst–Pack grid.[99] The structure was modeled as a (3 × 2 × 1) (111) slab in which four layers were adopted. The upper two layers of the slab were relaxed, and the lower two were fixed to their bulk constituents. A vacuum region of 15 Å was embedded, which is perpendicular to the surface to avoid the unwanted interaction between slabs and its periodic images. All atoms were fully relaxed until the Hellmann–Feynman force[100] on each atom converged to less than 0.05 eV/Å.

ASSOCIATED CONTENT

ⓢ Supporting Information

Phase diagrams of the Au−Pd−Ni ternary system and the Au−Pd binary system; SEM image of np-Au. This material is available free of charge via the Internet at http://pubs.acs.org/.

AUTHOR INFORMATION

Corresponding Author
*E-mail: mwchen@wpi-aimr.tohoku.ac.jp.

Notes
The authors declare no competing financial interest.

REFERENCES

(1) Somorjai, G. A.; Frei, H.; Park, J. Y. *J. Am. Chem. Soc.* **2009**, *131*, 16589−16605.

(2) Arico, A. S.; Bruce, P.; Scrosati, B.; Tarascon, J. M.; Van Schalkwijk, W. *Nat. Mater.* **2005**, *4*, 366−377.

(3) Manthiram, A.; Murugan, A. V.; Sarkar, A.; Muraliganth, T. *Energy Environ. Sci.* **2008**, *1*, 621−638.

(4) Rolison, D. R.; Long, R. W.; Lytle, J. C.; Fischer, A. E.; Rhodes, C. P.; McEvoy, T. M.; Bourga, M. E.; Lubers, A. M. *Chem. Soc. Rev.* **2009**, *38*, 226−252.

(5) Hou, J. B.; Shao, Y. Y.; Ellis, M. W.; Moore, R. B.; Yi, B. L. *Phys. Chem. Chem. Phys.* **2011**, *13*, 15384−15402.

(6) Acres, G. J. K. *J. Power Sources* **2001**, *100*, 60−66.

(7) Kua, J.; Goddard, W. A. *J. Am. Chem. Soc.* **1999**, *121*, 10928−10941.

(8) Du, W.; Mackenzie, K. E.; Milano, D. F.; Deskins, N. A.; Su, D.; Teng, X. *ACS Catal.* **2012**, *2*, 287−297.

(9) Antolini, E. *Mater. Chem. Phys.* **2003**, *78*, 563−573.

(10) Parsons, R.; VanderNoot, T. *J. Electroanal. Chem. Interfacial Electrochem.* **1988**, *257*, 9−45.

(11) Antolini, E. *J. Power Sources* **2007**, *170*, 1−12.

(12) Ribadeneira, E.; Hoyos, B. A. *J. Power Sources* **2008**, *180*, 238−242.

(13) Li, M.; Kowal, A.; Sasaki, K.; Marinkovic, N.; Su, D.; Korach, E.; Liu, P.; Adzic, R. R. *Electrochim. Acta* **2010**, *55*, 4331−4338.

(14) Tian, N.; Zhou, Z.-Y.; Sun, S.-G.; Ding, Y.; Wang, Z. L. *Science* **2007**, *316*, 732−735.

(15) Lamy, C.; Rousseau, S.; Belgsir, E. M.; Coutanceau, C.; Leger, J. M. *Electrochim. Acta* **2004**, *49*, 3901−3908.

(16) Zhou, W. J.; Li, W. Z.; Song, S. Q.; Zhou, Z. H.; Jiang, L. H.; Sun, G. Q.; Xin, Q.; Poulianitis, K.; Kontou, S.; Tsiakaras, P. *J. Power Sources* **2004**, *131*, 217−223.

(17) Vigier, F.; Coutanceau, C.; Perrard, A.; Belgsir, E. M.; Lamy, C. *J. Appl. Electrochem.* **2004**, *34*, 439−446.

(18) Riberio, J.; dos Anjos, D. M.; Kokoh, K. B.; Coutanceau, C.; Leger, J. M.; Olivi, P.; de Andrade, A. R.; Tremiliosi-Filho, G. *Electrochim. Acta* **2007**, *52*, 6997−7006.

(19) Jiang, L. H.; Sun, G. Q.; Zhou, Z. H.; Xin, Q. *Catal. Today* **2004**, *93−5*, 665−670.

(20) Kavanagh, R.; Cao, X. M.; Lin, W. F.; Hardacre, C.; Hu, P. *Angew. Chem., Int. Ed.* **2012**, *51*, 1572−1575.

(21) Ksar, F.; Surendran, G.; Ramos, L.; Keita, B.; Nadjo, L.; Prouzet, E.; Beaunier, P.; Hagège, A.; Audonnet, F.; Remita, H. *Chem. Mater.* **2009**, *21*, 1612−1617.

(22) Liu, J.; Ye, J.; Xu, C.; Jiang, S. P.; Tong, Y. *Electrochem. Commun.* **2007**, *9*, 2334−2339.

(23) Xu, C. W.; Wang, H.; Shen, P. K.; Jiang, S. P. *Adv. Mater.* **2007**, *19*, 4256−4259.

(24) Du, W.; Wang, Q.; Saxner, D.; Deskins, N. A.; Su, D.; Krzanowski, J. E.; Frenkel, A. I.; Teng, X. *J. Am. Chem. Soc.* **2011**, *133*, 15172−15183.

(25) Almeida, T. S.; Palma, L. M.; Leonello, P. H.; Morais, C.; Kokoh, K. B.; De Andrade, A. R. *J. Power Sources* **2012**, *215*, 53−62.

(26) Datta, J.; Dutta, A.; Biswas, M. *Electrochem. Commun.* **2012**, *20*, 56−59.

(27) Shen, S. Y.; Zhao, T. S.; Xu, J. B.; Li, Y. S. *Energy Environ. Sci.* **2011**, *4*, 1428−1433.

(28) Kim, I.; Han, O. H.; Chae, S. A.; Paik, Y.; Kwon, S. H.; Lee, K. S.; Sung, Y. E.; Kim, H. *Angew. Chem., Int. Ed.* **2011**, *50*, 2270−2274.

(29) Zhang, X. Y.; Lu, W.; Da, J. Y.; Wang, H. T.; Zhao, D. Y.; Webley, P. A. *Chem. Commun.* **2009**, 195−197.

(30) Kowal, A.; Li, M.; Shao, M.; Sasaki, K.; Vukmirovic, M. B.; Zhang, J.; Marinkovic, N. S.; Liu, P.; Frenkel, A. I.; Adzic, R. R. *Nat. Mater.* **2009**, *8*, 325−330.

(31) de Souza, J. P. I.; Queiroz, S. L.; Bergamaski, K.; Gonzalez, E. R.; Nart, F. C. *J. Phys. Chem. B* **2002**, *106*, 9825−9830.

(32) Rousseau, S.; Coutanceau, C.; Lamy, C.; Leger, J. M. *J. Power Sources* **2006**, *158*, 18−24.

(33) Prakash, G. K. S.; Krause, F. C.; Viva, F. A.; Narayanan, S. R.; Olah, G. A. *J. Power Sources* **2011**, *196*, 7967−7972.

(34) Li, W. Z.; Liang, C. H.; Zhou, W. J.; Qiu, J. S.; Zhou, Z. H.; Sun, G. Q.; Xin, Q. *J. Phys. Chem. B* **2003**, *107*, 6292−6299.

(35) Liu, Z. L.; Lin, X. H.; Lee, J. Y.; Zhang, W.; Han, M.; Gan, L. M. *Langmuir.* **2002**, *18*, 4054−4060.

(36) Seger, B.; Kamat, P. V. *J. Phys. Chem. C* **2009**, *113*, 7990−7995.

(37) Adzic, R. R.; Zhang, J.; Sasaki, K.; Vukmirovic, M. B.; Shao, M.; Wang, J. X.; Nilekar, A. U.; Mavrikakis, M.; Valerio, J. A.; Uribe, F. *Top. Catal.* **2007**, *46*, 249−262.

(38) Colon-Mercado, H. R.; Popov, B. N. *J. Power Sources* **2006**, *155*, 253−263.

(39) Ding, J.; Chan, K. Y.; Ren, J. W.; Xiao, F. S. *Electrochim. Acta* **2005**, *50*, 3131−3141.

(40) Antolini, E.; Passos, R. R.; Ticianelli, E. A. *Electrochim. Acta* **2002**, *48*, 263−270.

(41) Liu, Z. L.; Ling, X. Y.; Su, X. D.; Lee, J. Y. *J. Phys. Chem. B* **2004**, *108*, 8234−8240.

(42) Rolison, D. R.; Hagans, P. L.; Swider, K. E.; Long, J. W. *Langmuir.* **1999**, *15*, 774−779.

(43) Min, M. K.; Cho, J. H.; Cho, K. W.; Kim, H. *Electrochim. Acta* **2000**, *45*, 4211−4217.

(44) Steigerwalt, E. S.; Deluga, G. A.; Cliffel, D. E.; Lukehart, C. M. *J. Phys. Chem. B* **2001**, *105*, 8097−8101.

(45) Mu, Y. Y.; Liang, H. P.; Hu, J. S.; Jiang, L.; Wan, L. J. *J. Phys. Chem. B* **2005**, *109*, 22212−22216.

(46) Fernández, J. L.; Walsh, D. A.; Bard, A. J. *J. Am. Chem. Soc.* **2004**, *127*, 357−365.

(47) Zhu, Y. M.; Khan, Z.; Masel, R. I. *J. Power Sources* **2005**, *139*, 15−20.

(48) Antolini, E. *Energy Environ. Sci.* **2009**, *2*, 915−931.

(49) Evans, B. R.; O'Neill, H. M.; Malyvanh, V. P.; Lee, I.; Woodward, J. *Biosens. Bioelectron.* **2003**, *18*, 917−923.

(50) Yang, W. Q.; Yang, S. H.; Sun, W.; Sun, G. Q.; Xin, Q. *Electrochim. Acta* **2006**, *52*, 9−14.

(51) Bai, Z. Y.; Yang, L.; Li, L.; Lv, J.; Wang, K.; Zhang, J. *J. Phys. Chem. C* **2009**, *113*, 10568−10573.

(52) Jung, W. S.; Han, J. H.; Ha, S. *J. Power Sources* **2007**, *173*, 53−59.

(53) Ha, S.; Larsen, R.; Masel, R. I. *J. Power Sources* **2005**, *144*, 28−34.

(54) Lee, K.; Savadogo, O.; Ishihara, A.; Mitsushima, S.; Kamiya, N.; Ota, K. *J. Electrochem. Soc.* **2006**, *153*, A20−A24.

(55) Jayashree, R. S.; Spendelow, J. S.; Yeom, J.; Rastogi, C.; Shannon, M. A.; Kenis, P. J. A. *Electrochim. Acta* **2005**, *50*, 4674−4682.

(56) Fernandez, J. L.; Raghuveer, V.; Manthiram, A.; Bard, A. J. *J. Am. Chem. Soc.* **2005**, *127*, 13100−13101.

(57) Wang, X.; Tang, Y.; Gao, Y.; Lu, T. H. *J. Power Sources* **2008**, *175*, 784−788.

(58) Wang, D. L.; Lu, S. F.; Jiang, S. P. *Chem. Commun.* **2010**, *46*, 2058−2060.

(59) Cui, G.; Song, S.; Shen, P. K.; Kowal, A.; Bianchini, C. *J. Phys. Chem. C* **2009**, *113*, 15639−15642.

(60) Bianchini, C.; Shen, P. K. *Chem. Rev.* **2009**, *109*, 4183−4206.

(61) Chen, L.; Guo, H.; Fujita, T.; Hirata, A.; Zhang, W.; Inoue, A.; Chen, M. *Adv. Funct. Mater.* **2011**, *21*, 4364−4370.

(62) Shao, M.-H.; Sasaki, K.; Adzic, R. R. *J. Am. Chem. Soc.* **2006**, *128*, 3526−3527.

(63) Wang, X.; Kariuki, N.; Vaughey, J. T.; Goodpaster, J.; Kumar, R.; Myers, D. J. *J. Electrochem. Soc.* **2008**, *155*, B602−B609.

(64) Huang, Z.; Zhou, H.; Li, C.; Zeng, F.; Fu, C.; Kuang, Y. *J. Mater. Chem.* **2012**, *22*, 1781−1785.

(65) Lee, Y. W.; Kim, M.; Kim, Y.; Kang, S. W.; Lee, J.-H.; Han, S. W. *J. Phys. Chem. C* **2010**, *114*, 7689−7693.

(66) Hong, J. W.; Lee, Y. W.; Kim, M.; Kang, S. W.; Han, S. W. *Chem. Commun.* **2011**, *47*, 2553−2555.

(67) Cui, C.-H.; Yu, J.-W.; Li, H.-H.; Gao, M.-R.; Liang, H.-W.; Yu, S.-H. *ACS Nano* **2011**, *5*, 4211−4218.

(68) He, Q.; Chen, W.; Mukerjee, S.; Chen, S.; Laufek, F. *J. Power Sources* **2009**, *187*, 298−304.

(69) Liu, Z.; Zhao, B.; Guo, C.; Sun, Y.; Xu, F.; Yang, H.; Li, Z. *J. Phys. Chem. C* **2009**, *113*, 16766−16771.

(70) Ksar, F.; Ramos, L.; Keita, B.; Nadjo, L.; Beaunier, P.; Remita, H. *Chem. Mater.* **2009**, *21*, 3677−3683.

(71) Strasser, P.; Koh, S.; Anniyev, T.; Greeley, J.; More, K.; Yu, C.; Liu, Z.; Kaya, S.; Nordlund, D.; Ogasawara, H.; Toney, M. F.; Nilsson, A. *Nat. Chem.* **2010**, *2*, 454−460.

(72) Gao, F.; Goodman, D. W. *Chem. Soc. Rev.* **2012**, *41*, 8009−8020.

(73) Stamenkovic, V.; Mun, B. S.; Mayrhofer, K. J. J.; Ross, P. N.; Markovic, N. M.; Rossmeisl, J.; Greeley, J.; Nørskov, J. K. *Angew. Chem., Int. Ed.* **2006**, *45*, 2897−2901.

(74) Stamenkovic, V. R.; Fowler, B.; Mun, B. S.; Wang, G.; Ross, P. N.; Lucas, C. A.; Marković, N. M. *Science* **2007**, *315*, 493−497.

(75) Wang, C.; Chi, M.; Li, D.; Strmcnik, D.; van der Vliet, D.; Wang, G.; Komanicky, V.; Chang, K.-C.; Paulikas, A. P.; Tripkovic, D.; Pearson, J.; More, K. L.; Markovic, N. M.; Stamenkovic, V. R. *J. Am. Chem. Soc.* **2011**, *133*, 14396−14403.

(76) Friebel, D.; Viswanathan, V.; Miller, D. J.; Anniyev, T.; Ogasawara, H.; Larsen, A. H.; O'Grady, C. P.; Nørskov, J. K.; Nilsson, A. *J. Am. Chem. Soc.* **2012**, *134*, 9664−9671.

(77) Kibler, L. A.; El-Aziz, A. M.; Hoyer, R.; Kolb, D. M. *Angew. Chem., Int. Ed.* **2005**, *44*, 2080−2084.

(78) Mavrikakis, M.; Hammer, B.; Nørskov, J. K. *Phys. Rev. Lett.* **1998**, *81*, 2819−2822.

(79) Erlebacher, J.; Aziz, M. J.; Karma, A.; Dimitrov, N.; Sieradzki, K. *Nature* **2001**, *410*, 450−453.

(80) Erlebacher, J. *J. Electrochem. Soc.* **2004**, *151*, C614−C626.

(81) Erlebacher, J.; Seshadri, R. *MRS Bull.* **2009**, *34*, 561−568.

(82) Sieradzki, K.; Dimitrov, N.; Movrin, D.; McCall, C.; Vasiljevic, N.; Erlebacher, J. *J. Electrochem. Soc.* **2002**, *149*, B370−B377.

(83) Dursun, A.; Pugh, D. V.; Corcoran, S. G. *Electrochem. Solid-State Lett.* **2003**, *6*, B32−B34.

(84) Dursun, A.; Pugh, D. V.; Corcoran, S. G. *J. Electrochem. Soc.* **2005**, *152*, B65−B72.

(85) Snyder, J.; Asanithi, P.; Dalton, A. B.; Erlebacher, J. *Adv. Mater.* **2008**, *20*, 4883−4886.

(86) Fujita, T.; Guan, P. F.; McKenna, K.; Lang, X. Y.; Hirata, A.; Zhang, L.; Tokunaga, T.; Arai, S.; Yamamoto, Y.; Tanaka, N.; Ishikawa, Y.; Asao, N.; Erlebacher, J.; Chen, M. W. *Nat. Mater.* **2012**, *11*, 775−780.

(87) Koel, B. E.; Sellidj, A.; Paffett, M. T. *Phys. Rev. B* **1992**, *46*, 7846−7856.

(88) Xu, J. B.; Zhao, T. S.; Shen, S. Y.; Li, Y. S. *Int. J. Hydrogen Energy* **2010**, *35*, 6490−6500.

(89) Chen, L. Y.; Fujita, T.; Ding, Y.; Chen, M. W. *Adv. Funct. Mater.* **2010**, *20*, 2279−2285.

(90) Liu, J.; Ye, J.; Xu, C.; Jiang, S. P.; Tong, Y. *Electrochem. Commun.* **2007**, *9*, 2334−2339.

(91) Lee, Y. W.; Kim, M.; Kim, Y.; Kang, S. W.; Lee, J.-H.; Han, S. W. *J. Phys. Chem. C* **2010**, *114*, 7689−7693.

(92) Ksar, F.; Ramos, L.; Keita, B.; Nadjo, L.; Beaunier, P.; Remita, H. *Chem. Mater.* **2009**, *21*, 3677−3683.

(93) Kang, S. W.; Lee, Y. W.; Kim, M.; Hong, J. W.; Han, S. W. *Chem.—Asian J.* **2011**, *6*, 909−913.

(94) Lai, S. C. S.; Kleijn, S. E. F.; Öztürk, F. T. Z.; van Rees Vellinga, V. C.; Koning, J.; Rodriguez, P.; Koper, M. T. M. *Catal. Today* **2010**, *154*, 92−104.

(95) Chen, C. H.; Liou, W. J.; Lin, H. M.; Wu, S. H.; Borodzinski, A.; Stobinski, L.; Kedzierzawski, P. *Fuel Cells* **2010**, *10*, 227−233.

(96) Kresse, G.; Hafner, J. *Phys. Rev. B* **1993**, *47*, 558−561.
(97) Blöchl, P. E. *Phys. Rev. B* **1994**, *50*, 17953−17979.
(98) Perdew, J. P.; Burke, K.; Ernzerhof, M. *Phys. Rev. Lett.* **1996**, *77*, 3865−3868.
(99) Monkhorst, H. J.; Pack, J. D. *Phys. Rev. B* **1976**, *13*, 5188−5192.
(100) Feynman, R. P. *Phys. Rev.* **1939**, *56*, 340−343.